Analysis of Feasible Synchronverter Pole-placement Region to Facilitate Parameter Tuning

Shuan Dong, *Member, IEEE*, and Yu Christine Chen, *Member, IEEE*

***Abstract*—This paper derives in analytical closed form the feasible pole-placement region of the synchronverter active-power loop (APL) so as to eliminate all trial-and-error effort in parameter tuning. We consider the well-established setting of a reduced third-order APL model with two controller parameters that can be tuned freely. Thus, only two of the three APL poles can be specified independently in hopes of achieving desired system dynamics. Central to the presented derivation is the realization that the two specified poles must represent the dominant mode of the system. Otherwise the actual system dynamics may be dictated by the third unspecified pole, leading to unexpected or undesired dynamic behaviour. Numerical simulations involving the full-order synchronverter dynamical model and a modified New England 39-bus test system validate the analysis and the resulting region within which poles must be placed for actual system dynamics to match desired ones.**

***Index Terms*—Damping correction loop, grid-forming converter, parameter tuning, pole placement, synchronverter, virtual synchronous generator.**

NOMENCLATURE

D_f, D_p	Damping and frequency droop coefficients.
e_g, E_g	Synchronverter inner voltage and its line-to-line RMS value.
i_g	Synchronverter output current.
J_g	Inertia constant.
M_p, t_s	APL overshoot and settling time.
P_t, Q_t	Active- and reactive-power outputs.
$R_e + jX_e$	Transmission line impedance.
$R_s + jX_s$	L-type filter impedance.
$R_v + jX_v$	Virtual impedance.
s_1, s_2, s_3	Poles of synchronverter APL.
T_e, T_{ef}	Electromagnetic torque and its filtered value.
T_m	Synchronverter input torque.
u_{dc}	Dc-bus voltage.
u_t, U_t	Voltage at point of common coupling and its line-to-line RMS value.
u_∞, U_∞	Grid-side voltage and its line-to-line RMS value.
X_t	Total system reactance.
$\zeta^\star$	Desired APL damping ratio.
θ_g	Virtual rotor angle.
$\theta_{g\infty}$	Phase-angle difference between synchronverter inner voltage and grid-side voltage.
τ_f	Low-pass filter (LPF) time constant.
ψ_f, ψ_{ff}	Excitation flux and its filtered value.
ω_g	Virtual rotor rotating speed.
ω_n	APL natural frequency.
ω_N	Rated rotating speed.
ω_∞	Grid-side voltage angular frequency.
Ω_f	Feasible APL pole-placement region.
Superscript	
$\star$	Reference value.
$\circ$	Equilibrium value.
ss	Steady-state value.

S. Dong and Y. C. Chen are with the Department of Electrical and Computer Engineering at The University of British Columbia, Vancouver, BC, V6T 1Z4, Canada. Email: {shuan, chen}@ece.ubc.ca.

I. INTRODUCTION

GIVEN greater integration of power electronic-interfaced renewable energy systems with little to no inherent inertia, e.g., wind and solar, the traditional high-inertia synchronous generator-dominated power system is transitioning into a lower-inertia one augmented by power electronics [1]. This transformation brings forth numerous technical challenges to maintain power availability and quality. In order to address these problems, the concept of the virtual synchronous generator (VSG) has been proposed to leverage power-electronic converters to provide virtual inertia to the grid [2]–[16]. The core idea of the VSG is to design the voltage-source converter (VSC) controller so that it mimics the dynamics of a synchronous generator. In addition to contributing virtual inertia to the grid, the VSG is also able to adjust its active- and reactive-power outputs and provide timely frequency and voltage regulation.

Among the various instantiations of VSGs, the synchronverter is a representative design with concise controller structure [8]–[11]. Our previous work in [9] augments the original synchronverter design from [8] with the so-called *damping correction loop* so that its response speed can be adjusted freely without violating the steady-state frequency droop characteristic. Then, aimed at a simple procedure to tune the synchronverter parameters, [10] develops a method that directly computes parameter values that satisfy desired transient and steady-state behaviours [10]. Specifically, the tuning method in [10] leverages a reduced third-order model of the synchronverter active-power loop (APL) that captures pertinent system dynamics. However, since there are only two controller parameters that can be tuned freely, only two of the three poles can be specified independently, while the third depends on the placement of the first two. Consequently, the parameter tuning method in [10] achieves desired time-domain dynamic behaviour only if the two specified poles indeed represent the APL dominant mode. Otherwise, the synchronverter would display unexpected or undesired dynamics governed by the third pole. For this reason, as shown in Fig. 1, the method

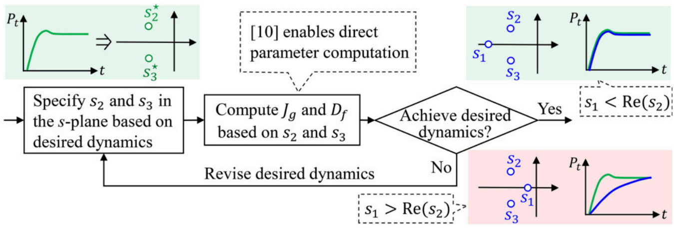

Fig. 1. The synchronverter parameter tuning method in [10] directly computes values for parameters J_g and D_f given two specified poles $s_2^\star$ and $s_3^\star$, which correspond to the desired time-domain dynamics. Since there are only two freely tuneable parameters, the third pole s_1 cannot be fixed independently and may actually play a more dominant role in the synchronverter dynamics than the specified ones s_2 and s_3, leading to undesired time-domain behaviour. This would then require additional trial-and-error effort to revise the desired time-domain dynamics.

in [10] requires repetitive trial-and-error effort to specify the two desired poles until they represent the dominant mode. In this paper, we improve the method in [10] by eliminating the potential trial-and-error effort involved with ill-advised choices of desired poles. Particularly, we provide analysis and develop precise conditions to determine the feasible pole-placement region, within which the two placed poles represent the APL dominant mode.[1]

In addition to the method developed in [10], lack of understanding of the feasible pole-placement region also complicates other VSG parameter tuning methods with cumbersome trial-and-error effort. For example, methods in [3]–[5] involve repeated specification of the natural frequency and the damping ratio for desired dominant poles to tune the VSG parameters with small-signal analysis before achieving desired dynamics. In view of this problem, numerous tuning methods endeavour to reduce or remove the required trial-and-error effort and facilitate the tuning procedure. For example, [6] leverages the virtual impedance to expand the feasible pole-placement region, and in so doing, reduces the trial-and-error effort of seeking feasible dominant pole locations. However, the adoption of virtual impedance may instead limit the feasible pole-placement region in some cases. Alternatively, the tuning methods in [11]–[16] do not pursue precise pole placement, and thus avoid some trial-and-error effort in the tuning procedure. The aforementioned tuning methods (at best) reduce the inherent trial-and-error effort involved instead of eliminating it altogether. However, the analytical characterization of the feasible pole-placement region *a priori* presented in this paper obviates all trial-and-error effort and significantly simplifies the VSG tuning procedure.

Given the literature reviewed above, this paper's contributions are as follows. First, we develop an analytical condition that helps to directly compute the range of the achievable synchronverter APL natural frequency with given APL damping ratio. Within the range predicted by this condition, we can indeed choose the desired APL natural frequency freely and achieve desired dynamics by computing parameters with the method in [10]. In this way, we completely eliminate all trial-and-error effort from the parameter tuning method in [10]. Furthermore, based on the developed condition, we derive analytical expressions that describe the feasible pole-placement region and visualize this region in the s-plane. These provide guidance for the synchronverter parameter tuning procedure and definitively delineate the achievable synchronverter dynamics. Finally, the analytical development leads to an improved parameter tuning method, which has the following advantages over existing methods:

1) *Predict achievable VSG dynamics.* The proposed method to compute the feasible pole-placement region enables analytical prediction of feasible VSG dynamics that can be achieved *prior to* parameter tuning. This is not possible in conventional methods like [7], [17]–[19].
2) *Reduce modelling and computation burden.* The proposed tuning method does not require potentially onerous derivation of the small-signal state-space system models as done in [4]–[6]. Also, it requires much less computational effort than previous tuning methods, e.g., [12], [20], that rely on optimization techniques.
3) *Realize desired VSG dynamics.* Compared to previous methods that tune parameters using Bode and Nyquist plots [14], [16], our proposed method realizes desired VSG dynamics with greater precision. This is because our method places pertinent dominant poles at specified locations in the s-plane that precisely correspond to desired VSG time-domain transient response.

The remainder of this paper is organized as follows. In Section II, we provide an overview for the synchronverter with damping correction loop and the associated parameter tuning method. Furthermore, via a numerical example, we highlight the necessity of obtaining the feasible pole-placement region prior to tuning the synchronverter parameters. Section III analytically derives the feasible pole-placement region and presents a modified parameter tuning method. Section IV provides numerical simulations that validate the analysis and derivation in Section III. Finally, in Section V, we offer concluding remarks and directions for future work.

II. Preliminaries

In this section, we provide an overview of the synchronverter design in [9] and the parameter tuning method in [10]. Also, via a numerical example, we motivate the need to modify the tuning method in [10] to eliminate all trial-and-error effort.

A. Synchronverter with Damping Correction Loop [9]

As shown in Fig. 2, the synchronverter consists of the active-power loop (APL) in Fig. 2(a), the reactive-power loop (RPL) in Fig. 2(b), and the interface to the grid in Fig. 2(c). We assume that the synchronverter dc-bus voltage u_{dc} remains constant. Also, the grid condition is assumed to be predominantly inductive, so the active- and reactive-power dynamics can be considered to be decoupled [16]. Let ψ_f and ψ_{ff}, respectively, denote the excitation flux generated from the RPL and its filtered value. In examining only the APL dynamics, we neglect the decoupled RPL dynamics by setting both ψ_f and ψ_{ff} to be their steady-state value ψ_f° [10]. Since the tuning method in [10] and the pole-placement region studied in this

[1]For ease of exposition, in the remainder of the paper, we refer to the pole(s) that represent the APL dominant mode interchangeably as *dominant pole(s)*.

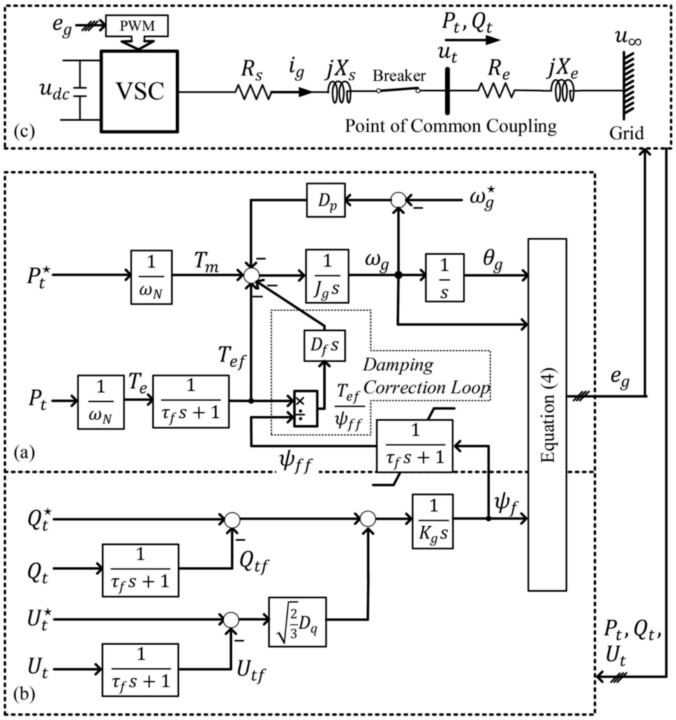

Fig. 2. Synchronverter augmented with damping correction loop [9]. (a) Synchronverter APL. (b) Synchronverter RPL. (c) Grid interface.

paper focus on the APL, below we describe only the APL and its interface to the grid. Interested readers may refer to Appendix A for details on the RPL.

1) Active-power Loop: The APL depicted in Fig. 2(a) provides freely adjustable inertia and damping, as its design is based on the swing equation augmented with the damping correction loop [9]. Let $\theta_{g\infty}$ denote the phase-angle difference between the inner voltage e_g and the grid-side voltage u_∞. Also let ω_g, T_e, and T_{ef}, respectively, denote the virtual rotor rotating speed, the electromagnetic torque, and the filtered electromagnetic torque. The APL dynamic model is as follows:

$$\frac{d\theta_{g\infty}}{dt} = \omega_g - \omega_\infty, \tag{1}$$

$$J_g \frac{d\omega_g}{dt} = T_m - T_{ef} - D_p(\omega_g - \omega_g^\star) - D_f \frac{d}{dt}\left(\frac{T_{ef}}{\psi_{\mathit{ff}}}\right), \tag{2}$$

$$\tau_f \frac{dT_{ef}}{dt} = -T_{ef} + T_e, \tag{3}$$

where J_g denotes the tuneable inertia constant, $T_m = \frac{P_t^\star}{\omega_N}$ represents the input torque with $P_t^\star$ being the active-power reference and ω_N the rated rotating speed, $\omega_g^\star$ is the reference rotating speed, and τ_f denotes the time constant of the low-pass filter (LPF). In (2), the term $D_p(\omega_g - \omega_g^\star)$ represents a simplified governor and achieves frequency-droop control, where D_p denotes the frequency droop coefficient. The damping correction loop $D_f \frac{d}{dt}\left(\frac{T_{ef}}{\psi_{\mathit{ff}}}\right)$ provides freely adjustable damping, since this term is in fact proportional to $\omega_g - \omega_\infty$, where D_f and ω_∞, respectively, denote the damping coefficient and the angular frequency of the grid-side voltage u_∞ [9]. We also note that the damping correction loop does not affect the steady-state frequency droop characteristics, since its output is zero at steady state.

2) Grid Interface: As shown in Fig. 2(c), the synchronverter is connected to the grid via an L-type filter $R_s + jX_s$ and a transmission line with impedance $R_e + jX_e$. Since the grid condition is assumed to be predominantly inductive, the total reactance $X_t := X_s + X_e \gg R_s + R_e$. Let ψ_f denote the excitation flux from the RPL, then the synchronverter inner voltage reference e_g is evaluated as follows:

$$e_g = \omega_g \psi_f \begin{bmatrix} \sin\theta_g & \sin\left(\theta - \frac{2\pi}{3}\right) & \sin\left(\theta + \frac{2\pi}{3}\right) \end{bmatrix}^{\mathrm{T}}, \tag{4}$$

and its line-to-line RMS value is $E_g = \sqrt{3/2}\,\omega_g \psi_f$. With e_g in place, the VSC is operated with pulse width modulation (PWM) technique. Let U_∞ denote the line-to-line RMS value of u_∞. Then the electromagnetic torque is given by

$$T_e = \frac{P_t}{\omega_N} \approx \sqrt{\frac{3}{2}} \frac{\psi_f U_\infty \sin\theta_{g\infty}}{X_t}, \tag{5}$$

where P_t denotes the active-power output [9].

Remark 1 (On Cascaded Voltage and Current Loops and Virtual Impedance Branch)**.** More detailed VSG models [21], which include the LCL filter, the cascaded voltage and current loops, and virtual impedance branch, can be reduced to the one in Fig. 2 via two considerations. First, the cascaded voltage and current loops (including the converter-side impedance $R_1 + jX_1$ of the LCL filter) can be approximated as unity gain blocks when tuning parameters or analyzing dynamics related to the output power [22]. The justification for this approximation is that the typical timescales of operation for the cascaded loops, in the range of 1–10 ms, are much smaller than those of the APL and RPL with 0.1–1 s [23]. Next, the virtual impedance branch with impedance $R_v + jX_v$ can be equivalently connected in series to the grid-side impedance $R_2 + jX_2$ of the LCL filter. Thus, by setting $R_s = R_v + R_2$ and $X_s = X_v + X_2$, the synchronverter in Fig. 2 and other LCL-filter-based VSG designs share similar output-power dynamics. We also note that assigning a positive virtual resistance R_v effectively suppresses potential VSG synchronous resonance, which is caused by small R/X ratio or sufficiently fast output-power dynamics [7], [24]. Since the required virtual resistance value R_v is typically much smaller than the total system reactance X_t, the predominantly inductive grid assumption in our paper still holds. ■

B. Parameter Tuning by Direct Computation [10]

As demonstrated in [10] and summarized above, the APL dynamics can be accurately captured by a third-order model, the block diagram of which is shown in Fig. 3. Furthermore, the third-order model has the following characteristic equation:

$$s^3 + bs^2 + Ks + d = 0, \tag{6}$$

where

$$b = \frac{J_g + \tau_f D_p}{\tau_f J_g}, \tag{7}$$

$$K = \frac{1}{\tau_f J_g}\left(D_p + D_f \sqrt{\frac{3}{2}} \frac{U_\infty \cos\theta_{g\infty}^\circ}{X_t}\right), \tag{8}$$

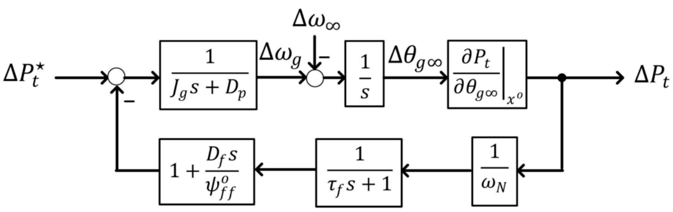

Fig. 3. Small-signal APL model.

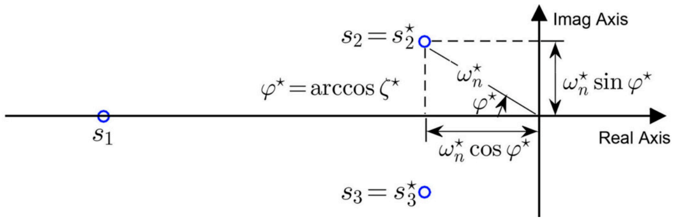

Fig. 4. Achieving desired APL dynamics by specifying $\omega_n^\star$ and $\zeta^\star$ for desired APL dominant pole locations $s_2^\star$ and $s_3^\star$ and directly computing parameters J_g and D_f with (13) and (14) [10].

$$d = \sqrt{\frac{3}{2}\frac{\psi_f^\circ U_\infty \cos\theta_{g\infty}^\circ}{\tau_f J_g X_t}}, \tag{9}$$

where superscript $\circ$ denotes the equilibrium value of the corresponding variable. We provide a brief sketch of how to obtain (6) in Appendix B. The three roots of (6), denoted by s_1, s_2, and s_3, represent the APL poles. Let $\omega_n^\star$ and $\zeta^\star$ denote the desired APL natural frequency and damping ratio, respectively. Then, as shown in Fig. 4, the desired locations for two of APL poles, s_2 and s_3, are specified as

$$s_2^\star = \omega_n^\star e^{j(\pi-\varphi^\star)} = -\omega_n^\star\cos\varphi^\star + j\omega_n^\star\sin\varphi^\star, \tag{10}$$

$$s_3^\star = \omega_n^\star e^{j(\pi+\varphi^\star)} = -\omega_n^\star\cos\varphi^\star - j\omega_n^\star\sin\varphi^\star, \tag{11}$$

respectively, where $\varphi^\star = \arccos\zeta^\star \in [0, \pi/2)$ rad. According to the model outlined in Section II-A, the APL has four control parameters that need to be specified: D_p, τ_f, J_g, and D_f. Among them, D_p is determined based on the local grid code as

$$D_p = \frac{\Delta T_m^{\mathrm{ss}}}{\Delta\omega_g^{\mathrm{ss}}}, \tag{12}$$

where $\Delta\omega_g^{\mathrm{ss}}$ represents the steady-state deviation of ω_g from its reference value $\omega_g^\star$, and ΔT_m^{ss} is the corresponding steady-state variation in the input torque T_m required by the grid code [8]. The time constant τ_f is chosen based on the required LPF noise rejection ability. The remaining two parameters, J_g and D_f, are conventionally tuned iteratively by repeatedly checking system poles under different parameter settings via small-signal analysis [9]. However, the iterative tuning method requires repeated evaluation of system poles and significant trial-and-error effort. To overcome the shortcomings of iterative methods, the method in [10] computes J_g and D_f directly based on the specified $\omega_n^\star$ and $\zeta^\star$ as follows:

$$J_g = \frac{\sqrt{\frac{3}{2}}\psi_f^\circ U_\infty\cos\theta_{g\infty}^\circ - \tau_f D_p X_t {\omega_n^\star}^2}{{\omega_n^\star}^2 X_t(1-2\tau_f\omega_n^\star\zeta^\star)}, \tag{13}$$

$$D_f = \frac{2\psi_f^\circ\zeta^\star}{\omega_n^\star} + \frac{\tau_f\psi_f^\circ}{1-2\tau_f\omega_n^\star\zeta^\star} - \sqrt{\frac{2}{3}}\frac{X_t D_p}{U_\infty\cos\theta_{g\infty}^\circ}\left(1+\frac{{\tau_f}^2{\omega_n^\star}^2}{1-2\tau_f\omega_n^\star\zeta^\star}\right). \tag{14}$$

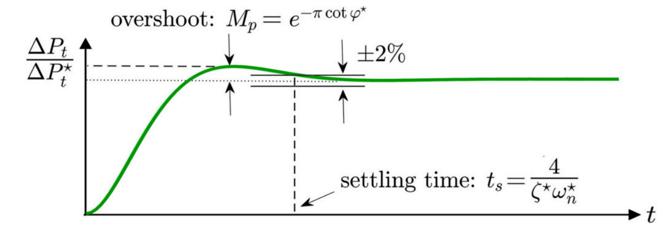

Fig. 5. APL time-domain step response with desired maximum relative overshoot M_p and settling time t_s.

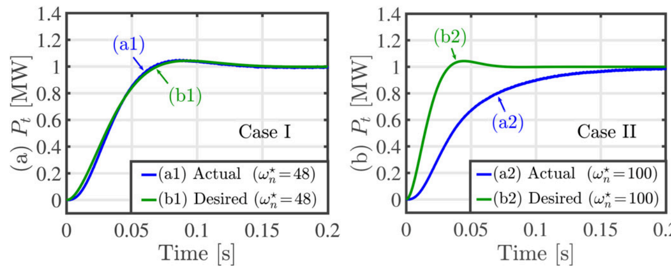

Fig. 6. Impact of $\omega_n^\star$ and $\zeta^\star$ on APL dynamics. (a) Case I: with $\omega_n^\star = 48$ and $\zeta^\star = 0.707$ desired APL dynamics are achieved by using parameters computed with (13) and (14). (b) Case II: with $\omega_n^\star = 100$ and $\zeta^\star = 0.707$, parameters computed with (13) and (14) do not result in desired dynamics.

With J_g and D_f computed from (13) and (14), as depicted in Fig. 4, we place two of APL poles, s_2 and s_3, at the desired pole locations, $s_2^\star$ and $s_3^\star$, respectively. By specifying two out of the three poles, as shown in Fig. 5, we aim to achieve APL time-domain dynamics with desired maximum relative overshoot M_p and settling time t_s given by, respectively, [25]

$$M_p = e^{-\pi\cot\varphi^\star}, \quad t_s = \frac{4}{\zeta^\star\omega_n^\star}. \tag{15}$$

Via a numerical example 1 below, we find that for certain pairs of $\omega_n^\star$ and $\zeta^\star$, we cannot achieve the desired APL dynamics with transient-response specifications according to (15).

Example 1 (Impact of Choice of $\omega_n^\star$ and $\zeta^\star$ on APL Dynamics)**.** In this example, we examine the impact of various settings for $\omega_n^\star$ and $\zeta^\star$ on actual APL dynamics. We use (13) and (14) to compute J_g and D_f based on specified $\omega_n^\star$ and $\zeta^\star$. Then using the PSCAD/EMTDC simulation software, we simulate the full-order system in Fig. 2 with the resulting values of J_g and D_f to obtain the actual APL step response to a change in $P_t^\star$. Note that the synchronverter simulation model fully considers the APL and RPL dynamics as well as the PWM switching sequence control. Assume that $D_p = 120$ N $\cdot$ m $\cdot$ s/rad according to local grid code, and all other parameter settings are reported in Appendix C. We consider two cases with $\omega_n^\star$ set to be 48 (Case I) and 100 rad/s (Case II). In both cases, we choose $\zeta^\star = 0.707$, which is the optimal damping ratio value that enables the APL to achieve fastest response with minimum overshoot. The actual APL step response (together with the desired APL step response with transient performance specifications in (15)) in Cases I and II are plotted in Fig. 6. As shown in

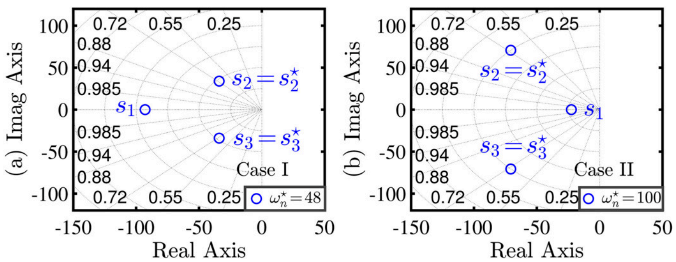

Fig. 7. Impact of $\omega_n^\star$ and $\zeta^\star$ on pole-placement results in the s-plane. (a) Case I: $\omega_n^\star = 48$, the parameters computed with (13) and (14) place s_2 and s_3 at their specified locations and the two placed poles represent the APL dominant mode; (b) Case II: $\omega_n^\star = 100$, the unspecified s_1, instead of s_2 and s_3, is in fact the APL dominant pole and dictates the APL dynamics.

Fig. 6(a), with $\omega_n^\star = 48$ (Case I), the actual APL step response (trace (a1)) matches well with the desired one characterized by (15) (trace (b1)). However, with $\omega_n^\star = 100\ \mathrm{rad/s}$ (Case II), as shown in Fig. 6(b), the actual APL step response (trace (a2)) is significantly slower than the desired one (trace (b2)). In this case, the desired APL dynamics are not achieved. ■

C. Problem Statement

As shown in Example 1, after specifying $\omega_n^\star$ and $\zeta^\star$ and computing J_g and D_f with (13) and (14), we may not achieve desired APL dynamics. The root cause of this problem can be identified by examining the specified poles s_2 and s_3 relative to the unspecified one s_1 in the s-plane. In Case I with $\omega_n^\star = 48$, as shown in Fig. 7(a), the two specified poles s_2 and s_3 are placed at their desired locations, and since $s_1 = -92.9 < \mathrm{Re}(s_2)$, s_2 and s_3 are the APL dominant poles and govern the APL dynamics. Thus, we achieve desired APL time-domain dynamics, as shown in Fig. 6(a). However, in Case II with $\omega_n^\star = 100$, as depicted in Fig. 7(b), although specified poles s_2 and s_3 are placed at their desire locations, the unspecified pole $s_1 = -22.5 > \mathrm{Re}(s_2)$, and s_1 becomes the APL dominant pole. Due to the influence of s_1, as shown in Fig. 6(b), the actual APL step response (trace (a2)) is much slower than the desired one (trace (b2)). In this case, we cannot achieve desired APL dynamics, and consequently the tuning procedure requires additional trial-and-error effort when specifying desired performance specifications. Thus, in order to completely eliminate potentially onerous trial-and-error effort, the tuning method in [10] should further determine the feasible choices of $\omega_n^\star$ and $\zeta^\star$, which ensure that s_2 and s_3 indeed represent the APL dominant mode upon parameter tuning.

III. Feasible Pole-placement Region

We present the main contribution of this paper: analytical characterization of the feasible pole-placement region. This enables us to determine the values of $\omega_n^\star$ and $\zeta^\star$ that ensure s_2 and s_3 are dominant poles *before* computing parameters J_g and D_f. In this way, the potentially burdensome process of repeatedly setting the desired APL poles is completely eliminated. For the specified APL poles to represent the APL dominant mode, the following condition must be satisfied:

$$s_1 < \mathrm{Re}(s_2) = \mathrm{Re}(s_3) = -\omega_n^\star \zeta^\star. \tag{16}$$

We derive the feasible pole-placement region that satisfies (16) in analytical closed form. We first derive the feasible range of $\omega_n^\star$ for a fixed $\zeta^\star$ (or equivalently $\varphi^\star$). The key observation is that depending on the value of D_p, there are three possible cases to consider. Then, by varying $\zeta^\star$ from 1 to 0 (or equivalently, varying $\varphi^\star$ from 0 to $\pi/2$ rad), we visualize the entire feasible pole-placement region in the s-plane, which also consists of three cases depending the value of D_p. Finally, based on the pole-placement region analysis, we improve the direct computation method in [10] by eliminating the trial-and-error effort needed to specify $\omega_n^\star$ and $\zeta^\star$.

A. Analytical Characterization

Here, we specify a particular value for $\zeta^\star$ and study the range of values that $\omega_n^\star$ can take to ensure s_2 and s_3 satisfy (16) and represent the APL dominant mode. To begin our analysis, we express s_1 as a function of $\omega_n^\star$ and $\zeta^\star$. Application of Vieta's formulas for (6) yields s_1 expressed as [26]

$$s_1 = -\frac{d}{s_2^\star s_3^\star} = -\frac{d}{{\omega_n^\star}^2}. \tag{17}$$

By substituting (13) into (9), and further substituting the resultant into (17), we express s_1 as the following function of $\omega_n^\star$ and $\zeta^\star$:

$$s_1(\omega_n^\star, \zeta^\star) = -\frac{M^2(2\tau_f\zeta^\star\omega_n^\star - 1)}{\tau_f\,(\omega_n^\star + M)\,(\omega_n^\star - M)}, \tag{18}$$

where

$$M = \sqrt{\sqrt{\frac{3}{2}}\frac{\psi_f^\circ U_\infty \cos\theta_{g\infty}^\circ}{D_p\tau_f X_t}}, \tag{19}$$

with the values of τ_f and D_p already set based on other design considerations mentioned in Section II-B. We note that according to (18), the value of s_1 is parametrized by the value taken by M. Also, since M is inversely proportional to $\sqrt{D_p}$, the range for $\omega_n^\star$ satisfying (16) similarly depends on the value of D_p. In order to delineate the feasible range of $\omega_n^\star$, we define an auxiliary variable $\mu \geq 0$, as follows:

$$\mu := \frac{1}{2\tau_f M} = \sqrt{\frac{D_p}{N}}, \tag{20}$$

where

$$N = \frac{2\sqrt{6}\tau_f\psi_f^\circ U_\infty\cos\theta_{g\infty}^\circ}{X_t}. \tag{21}$$

Next, we separately consider cases where $\mu = 0$ and $\mu > 0$ and characterize the range of $\omega_n^\star$ that satisfies (16) in each.

1) $\mu = 0$ ($D_p = 0$): The synchronverter is not required by the grid code to provide primary frequency regulation. With $D_p = 0$, the expression for s_1 in (18) simplifies as

$$s_1 = 2\,\omega_n^\star\zeta^\star - \frac{1}{\tau_f}. \tag{22}$$

By substituting (22) into (16), and bear in mind that $\omega_n^\star > 0$, we get the range of $\omega_n^\star$, which ensures that s_2 and s_3 are APL dominant poles, as follows:

$$\omega_n^\star \in \left(0,\ \frac{1}{3\tau_f\zeta^\star}\right). \tag{23}$$

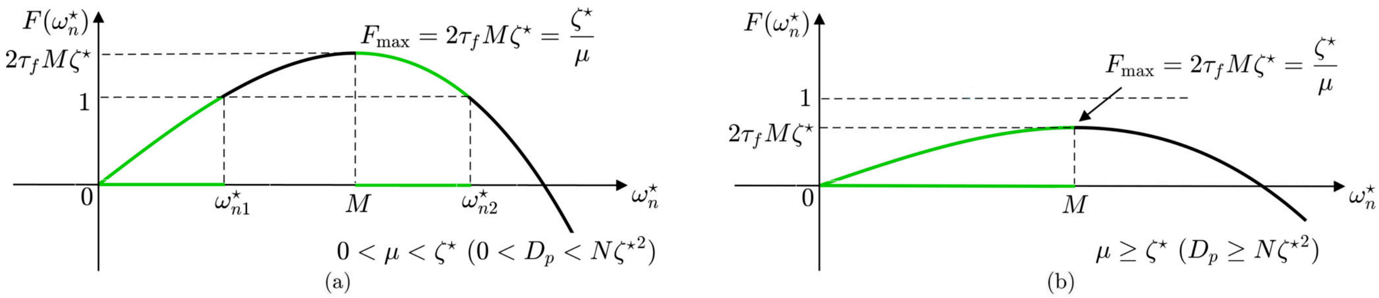

Fig. 8. Range of $\omega_n^\star$ which ensures that s_2 and s_3 are the APL dominant poles (i.e., $s_1 < \mathrm{Re}(s_2) = \mathrm{Re}(s_3)$) with (a) $0 < \mu < \zeta^\star$ $(0 < D_p < N\zeta^{\star 2})$ (b) $\mu \geq \zeta^\star$ $(D_p \geq N\zeta^{\star 2})$.

2) $\mu > 0$ ($D_p > 0$): The synchronverter is required by the local grid code to provide frequency regulation with $D_p > 0$. By substituting (18) into (16), we get

$$\frac{F(\omega_n^\star) - 1}{(\omega_n^\star + M)(\omega_n^\star - M)} > 0, \tag{24}$$

where

$$F(\omega_n^\star) := -\frac{\tau_f \zeta^\star {\omega_n^\star}^3}{M^2} + 3\tau_f \zeta^\star \omega_n^\star. \tag{25}$$

Recognizing that $\omega_n^\star > 0$ and $M > 0$ by definition, the conditions in (24) can be equivalently expressed as

$$0 < \omega_n^\star < M \text{ and } F(\omega_n^\star) < 1, \tag{26}$$

or

$$\omega_n^\star > M \text{ and } F(\omega_n^\star) > 1. \tag{27}$$

We leverage a graphical approach to solve the range of $\omega_n^\star$ from (26) and (27). Specifically, we plot $F(\omega_n^\star)$ in Fig. 8, and note that when $\omega_n^\star = M$, $F(\omega_n^\star)$ takes its maximum value as

$$F_{\max} = F(M) = 2\tau_f M\zeta^\star = \frac{\zeta^\star}{\mu}. \tag{28}$$

The relationship in (28) implies that the ratio between $\zeta^\star$ and μ determines the relationship between $F_{\max}$ and 1 and influences the feasible range of $\omega_n^\star$ solved from (26) and (27). Next, we characterize the feasible range of $\omega_n^\star$ with $0 < \mu < \zeta^\star$ and $\mu \geq \zeta^\star$.

(i) $0 < \mu < \zeta^\star$ $(0 < D_p < N\zeta^{\star 2})$: According to (28), $F_{\max} > 1$. As illustrated in Fig. 8(a), setting $F(\omega_n^\star) = 1$ yields two positive-valued roots, which we denote by $\omega_{n1}^\star$ and $\omega_{n2}^\star$ (with $0 < \omega_{n1}^\star < \omega_{n2}^\star$). Note that the solutions depend on $\zeta^\star$ and the roots can be solved from $F(\omega_n^\star) = 1$ via numerical methods or Cardano's formula [26]. Here, leveraging the intuition from Fig. 8(a), the solution of (26) and (27) is given by

$$\omega_n^\star \in (0,\, \omega_{n1}^\star) \cup (M,\, \omega_{n2}^\star)\,. \tag{29}$$

(ii) $\mu \geq \zeta^\star$ $(D_p \geq N\zeta^{\star 2})$: In this case, (28) implies that $F_{\max} \leq 1$, so $F(\omega_n^\star) \leq 1$ for all $\omega_n^\star > 0$, and (27) is never satisfied. Thus, as shown in Fig. 8(b), the solution of (26) is given by

$$\omega_n^\star \in (0,\, M)\,. \tag{30}$$

To sum up, for a particular $\zeta^\star = \cos\varphi^\star$, the range of $\omega_n^\star$ ensuring that s_2 and s_3 represent the APL dominant mode is given by

$$\omega_n^\star \in \begin{cases} \left(0,\, \dfrac{1}{3\tau_f\zeta^\star}\right), & \text{if } \mu = 0, \\ (0,\, \omega_{n1}^\star) \cup (M,\, \omega_{n2}^\star)\,, & \text{if } 0 < \mu < \zeta^\star, \\ (0,\, M)\,, & \text{if } \mu \geq \zeta^\star. \end{cases} \tag{31}$$

We refer to these conclusions on μ summarized in (31) as the μ-condition. Based on (15) and (31), we can indeed predict that the settling time of achievable APL dynamics is within the following range

$$t_s \in \begin{cases} (12\tau_f,\, +\infty)\,, & \text{if } \mu = 0, \\ \left(\dfrac{4}{\zeta^\star\omega_{n2}^\star},\, \dfrac{4}{\zeta^\star M}\right) \cup \left(\dfrac{4}{\zeta^\star\omega_{n1}^\star},\, +\infty\right), & \text{if } 0{<}\mu{<}\zeta^\star, \\ \left(\dfrac{4}{\zeta^\star M},\, +\infty\right), & \text{if } \mu \geq \zeta^\star. \end{cases} \tag{32}$$

Example 2 (Revisiting Example 1 with the μ-Condition)**.** In this example, we use the μ-condition to justify the impact of choice of $\omega_n^\star$ and $\zeta^\star$ on the pole-placement results observed in Example 1. Recall that $D_p = 120\ \mathrm{N \cdot m \cdot s/rad}$ and $\zeta^\star = 0.707$, so that $\mu = 0.84 > \zeta^\star$ according to (20). Also, M is computed to be 59.35 from (19). Thus, according to (31), setting $\omega_n^\star \in (0, 59.35)$ rad/s would ensure that s_2 and s_3 represent the APL dominant mode. In time-domain quantities, the achievable APL settling time t_s is within the range $(0.095, +\infty)$ s. In Case I, we set $\omega_n^\star$ to be $48 \in (0, 59.35)$ rad/s, and as shown in Fig. 7(a), (16) is satisfied and s_2 and s_3 are indeed the APL dominant poles as desired. However, in Case II, $\omega_n^\star = 100 \notin (0, 59.35)$ rad/s, and thus as depicted in Fig. 7(b), (16) does not hold and instead s_1 represents the APL dominant mode. ■

Remark 2 (Range of $\omega_n^\star$ to Ensure that $s_1 < m\mathrm{Re}(s_2)$, $m > 1$)**.** In order to achieve desired APL dynamics with greater precision, we may further limit the impact of s_1 by revising the condition in (16) to be $s_1 < m\mathrm{Re}(s_2)$, where $m > 1$. To this end, when specifying $\omega_n^\star$ before computing J_g and D_f, the feasible range of values that $\omega_n^\star$

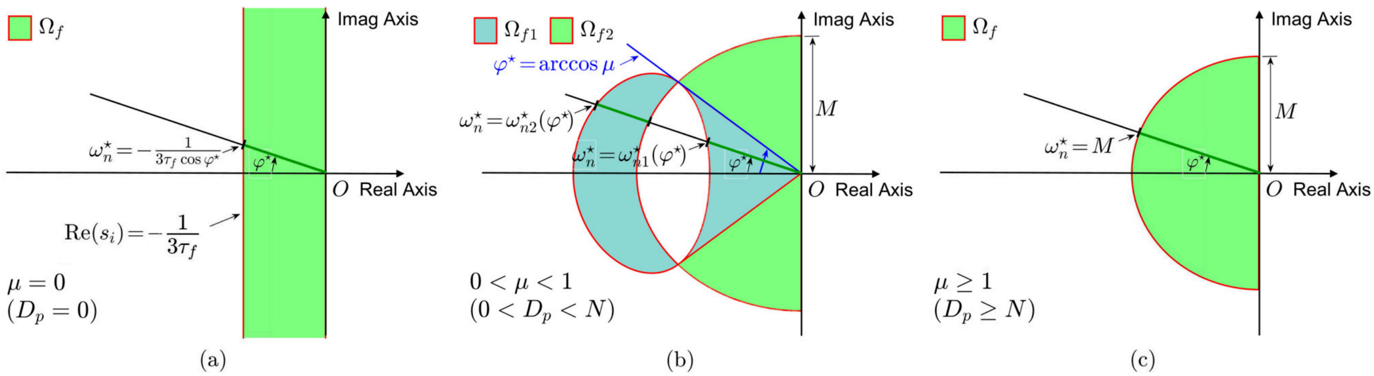

Fig. 9. Different feasible pole-placement regions for APL dominant poles s_2 and s_3 in the s-plane when (a) $\mu = 0$ ($D_p = 0$), (b) $0 < \mu < 1$ ($0 < D_p < N$), and (c) $\mu \geq 1$ ($D_p > N$).

can take is of the following form:

$$\omega_n^\star \in \begin{cases} \left(0,\, \dfrac{1}{(m+2)\tau_f\zeta^\star}\right), & \text{if } \mu = 0, \\ (0,\, \overline{\omega}_{n1}^\star) \cup (M,\, \overline{\omega}_{n2}^\star), & \text{if } 0 < \mu < \sqrt{\dfrac{(m+2)^3}{27m}}\zeta^\star, \\ (0,\, M), & \text{if } \mu \geq \sqrt{\dfrac{(m+2)^3}{27m}}\zeta^\star, \end{cases} \quad (33)$$

where $\overline{\omega}_{n1}^\star$ and $\overline{\omega}_{n2}^\star$ ($\overline{\omega}_{n1}^\star < \overline{\omega}_{n2}^\star$) are the two positive-valued roots of

$$-\frac{m\tau_f\zeta^\star {\omega_n^\star}^3}{M^2} + (m+2)\tau_f\zeta^\star\omega_n^\star = 1. \quad (34)$$

For brevity, we omit the derivation of (33) as it is similar to that of (31). ■

B. Visual Representation

Based on the feasible range of $\omega_n^\star$ for specific $\zeta^\star = \cos\varphi^\star$ in (31), we vary $\zeta^\star$ from 1 to 0, or equivalently vary $\varphi^\star$ from 0 to $\pi/2$, and visualize the entire feasible pole-placement region for the APL dominant poles s_2 and s_3 in the s-plane. There are three possibilities for the feasible pole-placement region of s_2 and s_3 depending on the value of μ, as shown in Fig. 9.

1) Pattern (a) with $\mu = 0$ ($D_p = 0$): Since (23) holds for all $\varphi^\star \in [0, \pi/2)$, the real parts of s_2 and s_3 satisfy

$$\mathrm{Re}(s_2) = \mathrm{Re}(s_3) = -\omega_n^\star\zeta^\star \in \left(-\frac{1}{3\tau_f}, 0\right). \quad (35)$$

Thus, as marked by the green colour in Fig. 9(a), the region in which we can place s_2 and s_3 as APL dominant poles is

$$\Omega_f = \left\{ z \in \mathbb{C} \,\middle|\, -\frac{1}{3\tau_f} < \mathrm{Re}(z) < 0 \right\}. \quad (36)$$

2) Pattern (b) with $0 < \mu < 1$ ($0 < D_p < N$): The feasible pole-placement region Ω_f for the APL dominant poles is given by the union of regions Ω_{f1} and Ω_{f2}, i.e., $\Omega_f = \Omega_{f1} \cup \Omega_{f2}$, which we describe separately below.

(i) Region Ω_{f1}: With $\varphi^\star$ varying from 0 to $\arccos\mu$, we have $0 < \mu < \cos\varphi^\star = \zeta^\star$. This corresponds to the second case summarized in (31), and thus as marked by the sea-green colour in Fig. 9(b), Ω_{f1} is given by

$$\Omega_{f1} = \left\{ z = \omega_n^\star e^{j(\pi \pm \varphi^\star)} \,\middle|\, 0 \leq \varphi^\star < \arccos\mu, 0 < \omega_n^\star < \omega_{n1}^\star(\varphi^\star) \text{ or } M < \omega_n^\star < \omega_{n2}^\star(\varphi^\star) \right\}. \quad (37)$$

where $\omega_{n1}^\star(\varphi^\star)$ and $\omega_{n2}^\star(\varphi^\star)$ ($0 < \omega_{n1}^\star(\varphi^\star) < \omega_{n2}^\star(\varphi^\star)$) are the two positive-valued roots of $F(\omega_n^\star) = 1$. Note that $\omega_{n1}^\star$ and $\omega_{n2}^\star$ are functions of $\varphi^\star$, since the function $F(\omega_n^\star)$ in (25) is parameterized by the value taken by $\zeta^\star$ or equivalently $\varphi^\star$.

(ii) Region Ω_{f2}: With $\varphi^\star$ varying from $\arccos\mu$ to $\pi/2$, we have $\mu \geq \cos\varphi^\star = \zeta^\star$. This corresponds to third case in (31). Also, based on (19), we note that M is independent of $\varphi^\star$. Thus, as shown by the two circle sectors shaded in green colour in Fig. 9(b), Ω_{f2} is given by

$$\Omega_{f2} = \left\{ z = \omega_n^\star e^{j(\pi \pm \varphi^\star)} \,\middle|\, \arccos\mu \leq \varphi^\star < \frac{\pi}{2}, 0 < \omega_n^\star < M \right\}. \quad (38)$$

3) Pattern (c) with $\mu \geq 1$ ($D_p \geq N$): For $\varphi^\star \in [0, \pi/2)$, we have $\mu \geq 1 \geq \cos\varphi^\star = \zeta^\star$. This corresponds to third case in (31). Accordingly, as marked by green colour in Fig. 9(c), the feasible pole-placement region for the APL dominant poles is given by

$$\Omega_f = \left\{ z = \omega_n^\star e^{j(\pi \pm \varphi^\star)} \,\middle|\, 0 \leq \varphi^\star < \frac{\pi}{2}, 0 < \omega_n^\star < M \right\}. \quad (39)$$

C. Updated Parameter Tuning Method

Based on the analysis of the feasible pole-placement region above, we improve the tuning method for the APL parameters D_p, τ_f, J_g, and D_f in Section II-B as follows. As before, we first compute D_p with (12) according to local grid code and further determine τ_f based on the LPF noise rejection requirements. With these, we solve the system equilibrium point and compute μ using (20). Then, we choose the desired damping ratio $\zeta^\star$ for the APL dominant mode. After that, we determine the desired natural frequency $\omega_n^\star$ in the range (31) (or (33) if $s_1 < m\mathrm{Re}(s_2)$, $m > 1$, is required) with due consideration for the desired APL response speed. Finally, we compute J_g and D_f according to (13) and (14). The revised method described above is depicted graphically in Fig. 10. Unlike the method in [10] portrayed in Fig. 1, we do not need to repetitively specify $\omega_n^\star$, and compute J_g and D_f until the APL poles s_2 and s_3 indeed represent the APL dominant

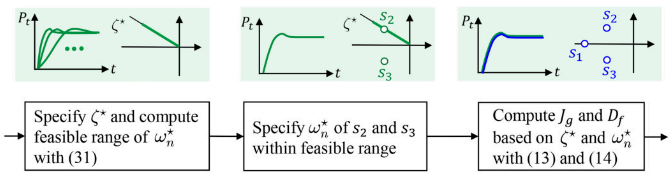

Fig. 10. Improved APL tuning method. Unlike the method in [10] depicted in Fig. 1, the updated tuning method is a linear procedure and requires no iterative trial-and-error effort when specifying the desired APL dynamics.

mode. In the next section, we verify the analytical development for the feasible pole-placement region via simulation studies.

Remark 3 (RPL Parameter Tuning Method)**.** Although the analysis and tuning procedure presented thus far focuses on the APL, a similar line of reasoning can be applied to parameter tuning for the RPL. Interested readers may refer to Appendix A for more details on the analysis and ensuing parameter tuning for the RPL. ■

IV. Case Studies

In this section, via time-domain simulations of the system in Fig. 2, we verify that by choosing $\omega_n^\star$ within the range specified by the derived μ-condition in (31), for a particular $\zeta^\star$, we indeed satisfy (16) and ensure that s_2 and s_3 represent the APL dominant mode. We also validate the feasible pole-placement region derived in Section III-B based on the μ-condition and visualized in the s-plane. Moreover, we demonstrate that the improved parameter tuning method effectively enables the synchronverter to achieve desired APL dynamics when it is connected to a benchmark test power system. The system under study in Sections IV-A and III-B is the synchronverter-connected system in Fig. 2 and values for all system parameters except D_p are reported in Appendix C. The system simulated in Section III-C is modified from the New England 39-bus test system reported in [27] and [28].

A. Verification of μ-Condition for Specific Choice of $\zeta^\star$

In order to verify the proposed μ-condition as summarized in (31), we choose APL damping ratio $\zeta^\star = 0.707$ and consider three cases: I) $D_p = 0\ \mathrm{N \cdot m \cdot s/rad}$, II) $D_p = 75\ \mathrm{N \cdot m \cdot s/rad}$, and III) $D_p = 120\ \mathrm{N \cdot m \cdot s/rad}$. According to (20), we get $\mu = 0$ in Case I, $0 < \mu < \zeta^\star$ in Case II, and $\mu > \zeta^\star$ in Case III, which correspond to the three possible options in (31). With these parameter settings, we compute the range of $\omega_n^\star$ satisfying (16) based on the μ-condition in (31) and shade the resulting regions in green colour in Figs. 11(a)–(c). To verify the range of feasible $\omega_n^\star$ obtained from (31), we vary $\omega_n^\star$ from 0 to $140\ \mathrm{rad/s}$, compute J_g and D_f using (13) and (14), substitute the resultant values into the APL characteristic equation (6), and solve for the actual APL poles s_1, s_2, and s_3 as the roots of (6). We plot s_1 and $\mathrm{Re}(s_2)$ with respect to $\omega_n^\star$ as the blue and red traces, respectively, in Figs. 11(a)–(c) for Cases I–III, respectively. Visual inspection of the red and blue traces in Figs. 11(a)–(c) reveals that indeed (16) is satisfied only when $\omega_n^\star$ lies within the green region, as predicted by (31). Thus, by specifying $\omega_n^\star$ within the

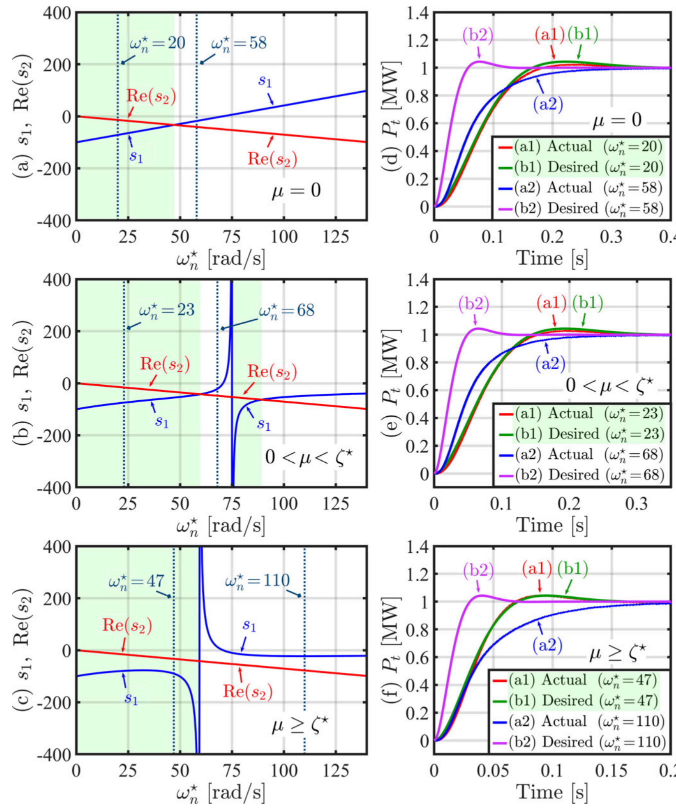

Fig. 11. Verification of μ-condition in (31) that specifies range of $\omega_n^\star$ for $\zeta^\star = 0.707$ when (a) $\mu = 0$ ($D_p = 0$), (b) $0 < \mu = 0.666 < \zeta^\star$ ($0 < D_p = 75 < N\zeta^{\star 2}$), and (c) $\mu = 0.843 \geq \zeta^\star$ ($D_p = 120 \geq N\zeta^{\star 2}$). Note that in Figs. 11(a)–(c), we use green shadow to mark the range of $\omega_n^\star$ computed from (31), and by choosing $\omega_n^\star$ within this range, we ensure that s_2 and s_3 represent the APL dominant poles and achieve desired time-domain APL dynamics after tuning synchronverter parameters with (13) and (14).

range predicted by the μ-condition, we ensure that s_2 and s_3 represent the APL dominant mode and subsequently achieve desired APL dynamic performance. Furthermore, the latter is also evident by checking the actual APL step response with different choices of $\omega_n^\star$ in Cases I–III against desired response satisfying (15) as shown in Figs. 11(d)–(f). Although we verify the μ-condition in (31) only for $\zeta^\star = 0.707$ above, we note that it holds for all possible $\zeta^\star \in (0, 1]$.

B. Verification of Feasible Pole-placement Region

In this study, we further verify that by placing s_2 and s_3 within the feasible pole-placement region, we automatically satisfy (16) and ensure that s_2 and s_3 are the APL dominant poles. As shown in Fig. 9, the feasible pole-placement region consists of three cases (Cases I–III) depending on the value of μ. We verify the three cases discussed in Section III-B by setting D_p to be 0, 90, and 200 $\mathrm{N \cdot m \cdot s/rad}$, which result in $\mu = 0$, $0 < \mu = 0.730 < 1$, and $\mu = 1.088 > 1$ in Cases I, II, and III, respectively. We compute the feasible pole-placement regions in Cases I–III with (36)–(39) and shade them with green or sea-green colours in Fig. 12. Then, we validate the pole-placement regions predicted in (36)–(39) by placing the APL poles s_2 and s_3 within and outside these regions and checking the actual resulting poles. In both Cases I and III,

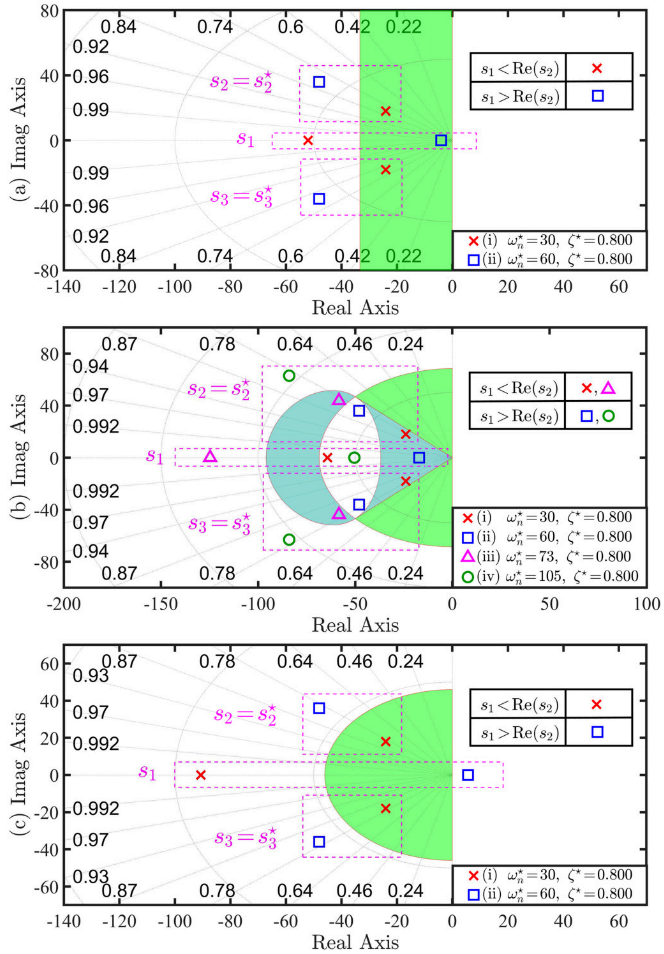

Fig. 12. Verification of feasible pole-placement region developed based on the μ-condition when (a) $\mu = 0$ ($D_p = 0$), (b) $0 < \mu = 0.730 < 1$ ($0 < D_p = 90 < N$), and (c) $\mu = 1.088 > 1$ ($D_p = 200 > N$). We shade the feasible pole-placement region with sea-green and green colours. By specifying the desired APL poles $s_2^\star$ and $s_3^\star$ within the feasible pole-placement region, (16) is satisfied and s_2 and s_3 indeed represent the APL dominant mode.

the poles s_2 and s_3 marked with $\times$ within the green region satisfy (16), while it is not true for those marked with $\square$ outside the green region. Similarly, in Case II, we have (16) for the APL poles marked with $\times$ and $\triangle$ within the feasible pole-placement region, while not for those marked with $\square$ and $\bigcirc$ outside the highlighted region. Based on these observations, we conclude that (16) is satisfied only if $s_2^\star$ and $s_3^\star$ are chosen to be within the feasible pole-placement region computed from (36)–(39). Thus, we validate the feasible pole-placement region visualized in the s-plane in Section III-B.

C. Verification in New England 39-Bus Test System

To further validate the feasible pole-placement region analysis as well as the updated tuning method in Section III, we implement it to tune the parameters for a synchronverter connected to a 39-bus test system, the one-line diagram of which is shown in Fig. 13. The test system is modified from the New England 39-bus system reported in [27] and [28], and as shown in Fig. 13, we replace the synchronous generator at Bus 30 with a synchronverter-controlled VSC with rated

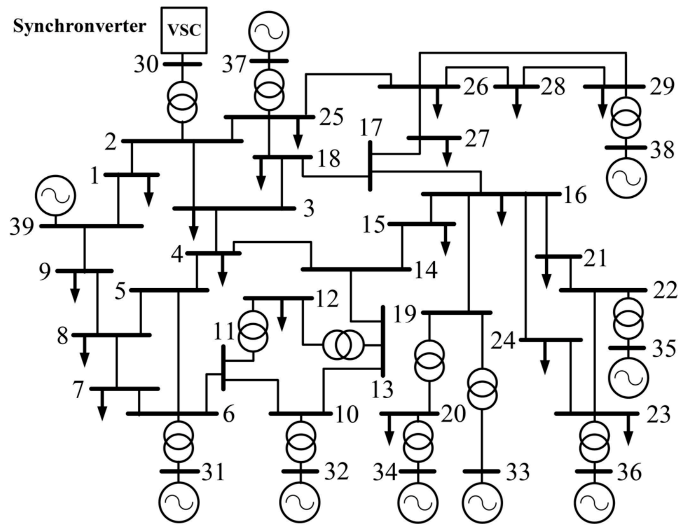

Fig. 13. Modified 39-bus test system used to validate the updated parameter tuning method.

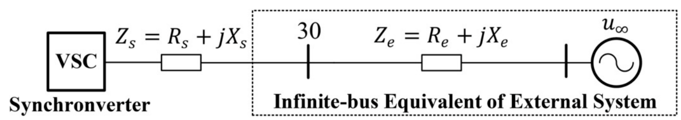

Fig. 14. Equivalent single-synchronverter infinite-bus system obtained from the 39-bus test system via network reduction.

capacity $S_N = 100$ MVA, rated AC voltage $U_N = 22.0$ kV, and switching frequency $f_{sw} = 5$ kHz. The synchronverter is connected to Bus 30 via an L-type filter with impedance $R_s + jX_s = 0.080 + j0.754\ \Omega$. Note that all generators at Buses 31-39 are equipped with exciters, steam turbines, and governors, which help to stabilize system voltages and achieve primary-frequency regulation.

Then, via network reduction techniques in [29], we compute an equivalent single-synchronverter infinite-bus system from the 39-bus system in Fig. 13. In the resultant equivalent two-bus system shown in Fig. 14, we have $Z_e \approx j0.150\ \Omega$ and $U_\infty = 22.7$ kV. Assume that the grid code does not require synchronverter to perform primary-frequency control, we have $D_p = 0$. Also, we set $\tau_f = 0.01$ s for LPFs to reduce measurement noise.

Next, we tune the APL parameters J_g and D_f following the updated procedure described in Section III-C. First, we set the desired APL damping ratio $\zeta^\star = 0.707$ and compute the system equilibrium. With $D_p = 0$, we have that $\mu = 0 < \zeta^\star$. Based on the μ-condition in (31), the APL natural frequency $\omega_n^\star \in (0, 47.1)$ rad/s, and correspondingly, the achievable APL settling time $t_s \in (0.12, +\infty)$ s. In accordance with its feasible range, we set the desired APL natural frequency $\omega_n^\star = 22.6$ rad/s, which corresponds to $t_s = 0.25$ s. Then using (13) and (14), we compute the APL parameters and get $J_g = 4.63 \times 10^3\ \mathrm{kg \cdot m^2}$ and $D_f = 4.07\ \mathrm{V \cdot s/rad}$.

With the computed synchronverter parameters in place, we model and simulate the synchronverter-connected 39-bus test system in Fig. 13 in the PSCAD/EMTDC simulation software. In this study, we increase the active-power reference $P_t^\star$ from 0

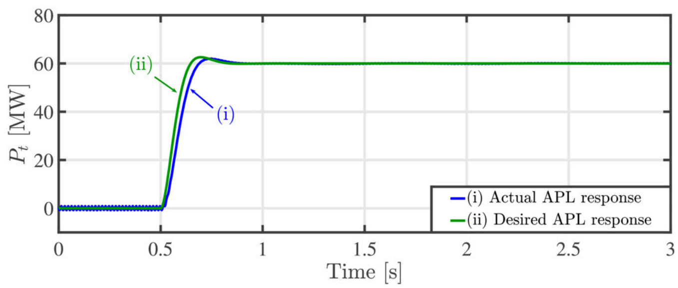

Fig. 15. Verification of proposed feasible pole-placement region analysis and updated tuning method in actual grid conditions.

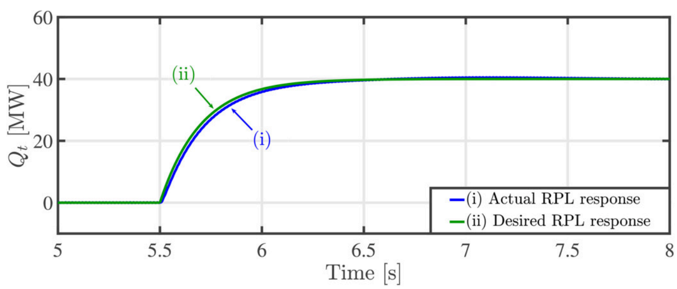

Fig. 16. Verification of RPL dynamics in actual grid conditions.

to 60 MW at $t = 0.5$ s. As shown in Fig. 15, the actual APL step response obtained from the simulation (trace (i)) indeed nearly matches the desired one with $\zeta^\star = 0.707$ and $\omega_n^\star = 22.6$ rad/s (trace (ii)). Thus, we demonstrate that the updated parameter tuning method, which considers the feasible pole-placement region analysis, tunes the synchronverter without any trial-and-error effort.

Remark 4 (Verification of RPL Dynamics)**.** Making use of the 39-bus test system, we verify the analysis for RPL dynamics in Appendix A. Assume that the synchronverter is not required to perform voltage-droop control, i.e., $D_q = 0$. Next, recall that LPF time constant $\tau_f = 0.01$ s, so the settling time t_s' of the RPL step response is freely adjustable within the range $(0.08, +\infty)$ s. Bearing this in mind, we choose the desired RPL dominant pole to be $s_4^\star = -5 \in \Omega_{f2}'$, which corresponds to $t_s' = 4/|s_4^\star| = 0.8$ s. Then according to (47), we get $K_g = 2.49 \times 10^6$ Var · rad/V. Finally, we simulate the system in PSCAD/EMTDC by increasing the reactive-power reference $Q_t^\star$ from 0 to 40 MVar at $t = 5.5$ s. As shown in Fig. 16, the actual RPL step response (trace (i)) matches well with the desired one with $t_s' = 0.8$ s (trace (ii)). ■

V. Concluding Remarks

In this paper, we derive the μ-condition to compute the range of the APL natural frequency $\omega_n^\star$ for chosen APL damping ratio $\zeta^\star$. Within the range of $\omega_n^\star$ predicted by the μ-condition, we are able to freely place the APL dominant poles and achieve desired APL dynamic performance. Thus, by incorporating the μ-condition into the tuning procedure of the synchronverter parameters, we eliminate the trial-and-error effort of repeatedly specifying $\omega_n^\star$ for the APL dominant mode, computing the APL parameters, and checking that s_2 and s_3 indeed represent the APL dominant mode. Based on the μ-condition, we visualize the feasible pole-placement region in the s-plane. Within this region, we are able to place the APL dominant poles freely and achieve desired APL dynamic performance. A similar line of reasoning is applied to determine the feasible range of achievable RPL dynamics and the corresponding parameters that lead to desired RPL dynamics. Compelling directions for future work include exploring the impact of the LPF filter on the feasible pole-placement region, computing the feasible pole-placement region of other VSG designs, and developing a systematic method of computing the feasible pole-placement region for other higher-order controller systems.

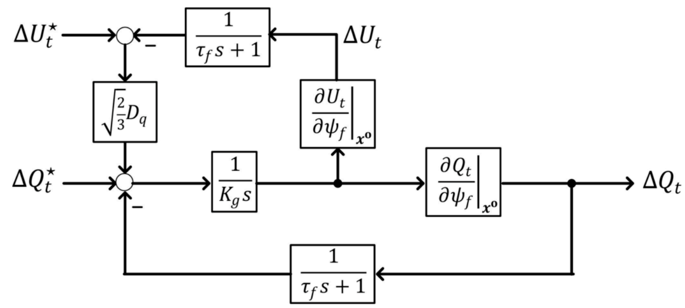

Fig. 17. Small-signal RPL model.

Appendix

A. Modelling, Analysis, and Tuning of RPL Dynamics

Modelling. According to Figs. 2(b) and (c), we can describe the RPL dynamics with the small-signal RPL model in Fig. 17, in which [9]

$$Q_t = \frac{X_e}{X_t^2}E_g^2 - \frac{X_s}{X_t^2}U_\infty^2 + \frac{X_s - X_e}{X_t^2}E_g U_\infty \cos\theta_{g\infty}, \quad (40)$$

$$U_t = \sqrt{\frac{X_e^2}{X_t^2}E_g^2 + \frac{X_s^2}{X_t^2}U_\infty^2 + \frac{2X_e X_s}{X_t^2}E_g U_\infty \cos\theta_{g\infty}}. \quad (41)$$

Then, leveraging Mason's gain formula [30], we get the RPL transfer function model as follows

$$\Delta Q_t = G_3(s)\Delta Q_t^\star + G_4(s)\Delta U_t^\star, \quad (42)$$

where $G_3(s)$ and $G_4(s)$, respectively, describe the dynamics in ΔQ_t with respect to $\Delta Q_t^\star$ and $\Delta U_t^\star$. In (42), we note that $G_3(s)$ and $G_4(s)$ share the following second-order characteristic equation

$$1 + Ks\left(s + \frac{1}{\tau_f}\right) = 0, \quad (43)$$

where

$$K := \frac{K_g \tau_f}{\frac{\partial Q_t}{\partial \psi_f}\big|_{x^\circ} + D_q\sqrt{\frac{2}{3}}\frac{\partial U_t}{\partial \psi_f}\big|_{x^\circ}} \propto K_g. \quad (44)$$

Analysis. Let s_4 and s_5, where $\mathrm{Re}(s_5) \le \mathrm{Re}(s_4)$, denote the two roots of the RPL characteristic equation (43). By varying K from 0 to $+\infty$, we plot the root loci patterns of (43) in Fig. 18. According to Fig. 18, the feasible RPL

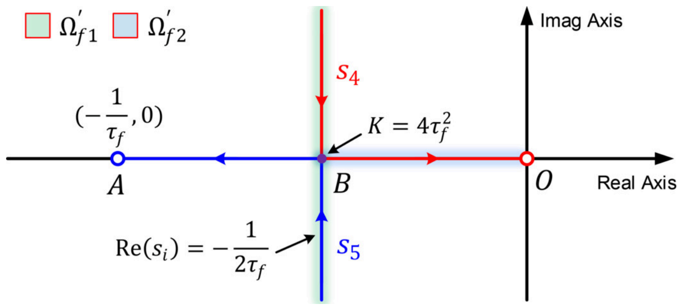

Fig. 18. Root loci patterns of $1 + Ks\left(s + \frac{1}{\tau_f}\right) = 0$ in the s-plane.

pole-placement region Ω'_f is the union of two regions, i.e., $\Omega'_f = \Omega'_{f1} \cup \Omega'_{f2}$, which we describe separately below.

1) $K \in (0, 4\tau_f^2]$: As shown in Fig. 18, increasing K from 0 to $4\tau_f^2$ makes s_4 and s_5 move toward each other along the line $\mathrm{Re}(s_i) = -1/(2\tau_f)$ until they meet at the point B, i.e., $(-1/(2\tau_f), 0)$, on the real axis. Thus, the first part of the feasible RPL pole-placement region, in which we can place the RPL dominant poles s_4 and s_5 freely, is along the line described by

$$\Omega'_{f1} = \left\{ z \in \mathbb{C} \,\middle|\, \mathrm{Re}(z) = -\frac{1}{2\tau_f} \right\}. \tag{45}$$

In the time domain, the settling time t'_s of the RPL step response is fixed at $t'_s = 4/|\mathrm{Re}(s_4)| = 8\tau_f$ while the overshoot remains adjustable.

2) $K \in (4\tau_f^2, +\infty)$: As shown in Fig. 18, increasing K from $4\tau_f^2$ to $+\infty$ makes s_4 and s_5 move away from each other along the real axis until they, respectively, arrive at points A and O. In this case, we have $s_5 < s_4$ and so s_4 dominates the RPL dynamics. Thus, the second part of the feasible RPL pole-placement region, in which we can place the RPL dominant pole s_4 freely, is the segment $\overline{BO}$, i.e.,

$$\Omega'_{f2} = \left\{ z \in \mathbb{R} \,\middle|\, -\frac{1}{2\tau_f} < z < 0 \right\}. \tag{46}$$

In the time domain, the settling time t'_s can be freely adjusted within $(8\tau_f, +\infty)$ and the RPL dynamics are overdamped.

Tuning. Based on the analysis above, we recommend tuning the synchronverter RPL by placing s_4 within the region Ω'_{f2} delineated in (46). In this way, the RPL response is freely adjustable and also well damped. Let $s_4^\star$ denote the desired location of s_4 in the s-plane, substitute $s_4 = s_4^\star$ and (44) into (43), and we get

$$K_g = -\frac{\frac{\partial Q_t}{\partial \psi_f}\big|_{\boldsymbol{x}^\circ} + D_q\sqrt{\frac{2}{3}}\frac{\partial U_t}{\partial \psi_f}\big|_{\boldsymbol{x}^\circ}}{s_4^\star(\tau_f s_4^\star + 1)}. \tag{47}$$

Recall that the voltage-droop constant D_q is determined based on the grid code, we can directly compute the remaining parameter K_g according to (47). In this way, we achieve RPL time-domain dynamics with $t'_s = 4/|s_4^\star|$ [25].

B. Small-signal APL Model

The APL dynamics are sufficiently described by (1)–(3) and (5). Let $\Delta(\cdot)$ denote small-signal perturbations in variable $(\cdot)$. Note that $\omega_g^\star$ is a reference value for ω_g and remains fixed, i.e., $\Delta\omega_g^\star = 0$. Thereafter, by linearizing (1)–(3) and (5) around the system equilibrium point, taking the Laplace transformation of the resultant, we can obtain the expression for $\Delta\theta_{g\infty}$ (see Section III in [10]). Finally, substitution of the expression for $\Delta\theta_{g\infty}$ into the linearized version of (5) yields the following small-signal third-order APL model [10]:

$$\begin{aligned}\Delta P_t &= \frac{d \cdot (\tau_f s + 1) \cdot (\Delta P_t^\star - \omega_N (J_g s + D_p)\Delta\omega_\infty)}{s^3 + bs^2 + Ks + d} \\ &=: G_1(s)\Delta P_t^\star + G_2(s)\Delta\omega_\infty,\end{aligned} \tag{48}$$

where b, K, and d are given by (7)–(9), respectively. Note that the third-order APL model in (48) considers the LPF dynamics in (3), and thus captures the APL dynamics with high accuracy, as verified in [10].

C. Parameters of Synchronverter-connected System in Fig. 2

$R_s = 0.741\ \Omega$, $L_s = 20$ mH, $R_e = 0.0\ \Omega$, $L_e = 38.5$ mH, $\tau_f = 0.01$ s, $D_p = 120\ \mathrm{N \cdot m \cdot s/rad}$, $\omega_N = \omega_g^\star = 376.99$ rad/s, $U_\infty = 6.6$ kV, $u_{dc} = 13$ kV, rated grid frequency is 60 Hz, rated ac side voltage is 6.6 kV, and rated synchronverter capacity is 1 MVA.

References

[1] F. Milano, F. Dörfler, G. Hug, D. J. Hill, and G. Verbič, "Foundations and challenges of low-inertia systems," in *Proc. 20th Power Syst. Comput. Conf.*, 2018, pp. 1–25.

[2] H. P. Beck and R. Hesse, "Virtual synchronous machine," in *Proc. 9th Int. Conf. Elect. Power Quality Util.*, 2007, pp. 1–6.

[3] J. Liu, Y. Miura, and T. Ise, "Fixed-parameter damping methods of virtual synchronous generator control using state feedback," *IEEE Access*, vol. 7, pp. 99 177–99 190, Jul. 2019.

[4] F. Gao and M. R. Iravani, "A control strategy for a distributed generation unit in grid-connected and autonomous modes of operation," *IEEE Trans. Power Del.*, vol. 23, no. 2, pp. 850–859, Apr. 2008.

[5] S. D'Arco, J. A. Suul, and O. B. Fosso, "Automatic tuning of cascaded controllers for power converters using eigenvalue parametric sensitivities," *IEEE Trans. Ind. Applicat.*, vol. 51, no. 2, pp. 1743–1753, 2014.

[6] A. Rodríguez-Cabero, J. Roldán-Pérez, and M. Prodanovic, "Virtual impedance design considerations for virtual synchronous machines in weak grids," *IEEE J. Emerg. Sel. Topics Power Electron.*, vol. 8, no. 2, pp. 1477–1489, Jun. 2020.

[7] L. Zhang, L. Harnefors, and H. P. Nee, "Power-synchronization control of grid-connected voltage-source converters," *IEEE Trans. Power Syst.*, vol. 25, no. 2, pp. 809–820, May 2010.

[8] Q.-C. Zhong and G. Weiss, "Synchronverters: Inverters that mimic synchronous generators," *IEEE Trans. Ind. Electron.*, vol. 58, no. 4, pp. 1259–1267, Apr. 2011.

[9] S. Dong and Y. C. Chen, "Adjusting synchronverter dynamic response speed via damping correction loop," *IEEE Trans. Energy Convers.*, vol. 32, no. 2, pp. 608–619, Jun. 2017.

[10] S. Dong and Y. C. Chen, "A method to directly compute synchronverter parameters for desired dynamic response," *IEEE Trans. Energy Convers.*, vol. 33, no. 2, pp. 814–825, Jun. 2018.

[11] R. Rosso, J. Cassoli, G. Buticchi, S. Engelken, and M. Liserre, "Robust stability analysis of LCL filter based synchronverter under different grid conditions," *IEEE Trans. Power Electron.*, vol. 34, no. 6, pp. 5842–5853, 2018.

[12] R. Aouini, B. Marinescu, K. B. Kilani, and M. Elleuch, "Synchronverter-based emulation and control of HVDC transmission," *IEEE Trans. Power Syst.*, vol. 31, no. 1, pp. 278–286, Jan. 2016.

[13] Y. Cao *et al.*, "A virtual synchronous generator control strategy for VSC-MTDC systems," *IEEE Trans. Energy Convers.*, vol. 33, no. 2, pp. 750–761, 2017.

[14] H. Xu, C. Yu, C. Liu, Q. Wang, and X. Zhang, "An improved virtual inertia algorithm of virtual synchronous generator," *J. Mod. Power Syst. Clean Energy*, vol. 8, no. 2, pp. 377–386, Mar. 2020.

[15] L. Huang, H. Xin, H. Yang, Z. Wang, and H. Xie, "Interconnecting very weak ac systems by multiterminal VSC-HVDC links with a unified virtual synchronous control," *IEEE Trans. Emerg. Sel. Topics Power Electron.*, vol. 6, no. 3, pp. 1041–1053, Sep. 2018.

[16] H. Wu *et al.*, "Small-signal modeling and parameters design for virtual synchronous generators," *IEEE Trans. Ind. Electron.*, vol. 63, no. 7, pp. 4292–4303, Jul. 2016.

[17] X. Quan *et al.*, "Photovoltaic synchronous generator: Architecture and control strategy for a grid-forming pv energy system," *IEEE Trans. Emerg. Sel. Topics Power Electron.*, vol. 8, no. 2, pp. 936–948, Jun. 2020.

[18] L. Harnefors, M. Hinkkanen, U. Riaz, F. M. M. Rahman, and L. Zhang, "Robust analytic design of power-synchronization control," *IEEE Trans. Ind. Electron.*, vol. 66, no. 8, pp. 5810–5819, Aug. 2019.

[19] Y. Du, J. M. Guerrero, L. Chang, J. Su, and M. Mao, "Modeling, analysis, and design of a frequency-droop-based virtual synchronous generator for microgrid applications," in *Proc. IEEE ECCE Asia Downunder*, 2013, pp. 643–649.

[20] M. Pourmohammad, M. Toulabi, and A. M. Ranjbar, "Application of state feedback controller to insure robust d-stable operation of virtual synchronous generators," *IEEE Trans. Energy Convers.*, to be published.

[21] S. D'Arco, J. A. Suul, and O. B. Fosso, "A virtual synchronous machine implementation for distributed control of power converters in smartgrids," *Electr. Power Syst. Res.*, vol. 122, pp. 180–197, 2015.

[22] D. Pan, X. Wang, F. Liu, and R. Shi, "Transient stability of voltage-source converters with grid-forming control: A design-oriented study," *IEEE Trans. Emerg. Sel. Topics Power Electron.*, vol. 8, no. 2, pp. 1019–1033, Jun. 2020.

[23] H. Wu and X. Wang, "Design-oriented transient stability analysis of grid-connected converters with power synchronization control," *IEEE Trans. Ind. Electron.*, vol. 66, no. 8, pp. 6473–6482, Aug. 2019.

[24] J. Wang, Y. Wang, Y. Gu, W. Li, and X. He, "Synchronous frequency resonance of virtual synchronous generators and damping control," in *Proc. 9th Int. Conf. Power Electron./ECCE Asia*, 2015, pp. 1011–1016.

[25] H. Ozbay, *Introduction to Feedback Control Theory*. New York: CRC Press, 1999.

[26] J. W. Harris and H. Stöcker, *Handbook of Mathematics and Computational Science*. New York: Springer-Verlag, 1998.

[27] T. Athay, R. Podmore, and S. Virmani, "A practical method for the direct analysis of transient stability," *IEEE Trans. Power App. Syst.*, vol. PAS-98, no. 2, pp. 573–584, Mar. 1979.

[28] M. A. Pai, *Energy Function Analysis for Power System Stability*. Norwell, MA: Kluwer, 1989.

[29] G. J. Berg and A. Ghafurian, "Representation of coherency-based equivalents in transient stability studies," *Electric Power Syst. Res.*, vol. 6, no. 4, pp. 235–241, Dec. 1983.

[30] F. Golnaraghi and B. Kuo, *Automatic Control Systems*, 9th ed. New York: Wiley, 2010.

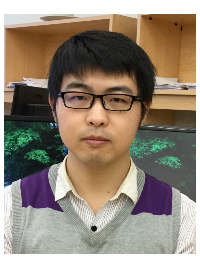

Shuan Dong (S'16–M'20) received the B.S. degree in electrical engineering from Tianjin University, Tianjin, China in 2012, the M.S. degree in renewable energy from China Electric Power Research Institute, Beijing, China, in 2015, and the Ph.D. degree in electrical engineering from The University of British Columbia, Vancouver, BC, Canada in 2019, respectively.

His research interests include HVDC technology and renewable energy integration in power systems.

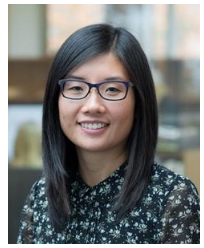

Yu Christine Chen (S'10–M'15) received the B.A.Sc. degree in engineering science from the University of Toronto, Toronto, ON, Canada, in 2009, and the M.S. and Ph.D. degrees in electrical engineering from the University of Illinois at Urbana-Champaign, Urbana, IL, USA, in 2011 and 2014, respectively.

She is currently an Assistant Professor with the Department of Electrical and Computer Engineering, The University of British Columbia, Vancouver, BC, Canada, where she is affiliated with the Electric Power and Energy Systems Group. Her research interests include power system analysis, monitoring, and control. Christine presently serves as Editors for the *IEEE Transactions on Energy Conversion* and the *IEEE Transactions on Power Systems*.